Original Article

Institution of MECHANICAL ENGINEERS
Journal of MECHANICAL ENGINEERING SCIENCE

Proc IMechE Part C:
J Mechanical Engineering Science
0(0) 1–11

DOI: 10.1177/0954406218822013
journals.sagepub.com/home/pic
SAGE

A hybrid continuum robot based on pneumatic muscles with embedded elastic rods

Cijing Sun[1], Lisha Chen[2], Jinguo Liu[3], Jian S Dai[1,4] and Rongjie Kang[1]

Abstract

Continuum robots have attracted increasing attention in recent years due to their intrinsic compliance and safety. Nevertheless, the use of structure compliance may lead to reduction of stiffness and positioning precision. This paper presents a novel design of a hybrid continuum robot whose actuators are composed of pneumatic muscles and embedded elastic rods. Such robot can switch drive modes between large-scale movement and fine adjustment of position by employing a locking mechanism to change its stiffness. A three-dimensional static model of the robot is presented using an improved Kirchhoff rod theory, where elastic deformation of the robot is accounted for from an optimal control point of view via minimal total potential energy principle. Experiments were carried out to validate the static model and to test the stiffness and precision of the robot. This work provides a possible way to strengthen the control precision of a continuum robot with compliant structure.

Keywords

Continuum robots, hybrid actuation, pneumatic muscles, elastic rods, variable stiffness, statics model

Date received: 29 June 2018; accepted: 22 October 2018

Introduction

In recent years, applications of robots are not only confined in industrial production, but also extended to unstructured environments such as disaster rescue, space exploration, minimally invasive surgery, etc.[1] When facing these complex and unstructured environments, traditional rigid robots are incompetent due to their limited degrees of freedom (DOF) and low compliance. In contrast, continuum robots with intrinsic compliance have attracted increasing attention as they are more suitable for operations requiring for high dexterity, adaptability and hyper-redundant DOF.[2]

To date, numerous continuum robots have been proposed. Menciassi et al.[3] designed a worm-like crawling robot actuated by shape memory alloy (SMA). Shintake et al.[4] presented a versatile soft gripper based on electroactive polymer (EAP) actuators. Yuk et al.[5] developed a transparent continuum robot using hydraulic hydrogel actuators that can be optically and sonically camouflaged in water. Jones and Walker[2] and Walker et al.[6] developed several pneumatically actuated continuum robots inspired by elephant trunks and cephalopods. Kang et al.[7] presented a multi-segmented continuum robot using extensible pneumatic muscles. Robertson and Paik[8] developed a vacuum-powered continuum robot using negative pressure to achieve motions. Calisti et al.[9] designed a tendon-driven continuum robot that is capable of manipulation and locomotion. Cao et al.[10] investigated the workspace of a tendon-driven continuum robot and identified the mechanical interference between its tendons and central backbone. Xu and Simaan[11] utilized elastic Ni–Ti rods instead of tendons to drive a continuum robot which has higher stiffness in comparison with tendon-driven ones. Through reviewing the previous designs, it is found that single actuation method mentioned above is not

[1]Key Laboratory of Mechanism Theory and Equipment Design of the Ministry of Education, International Centre for Advanced Mechanisms and Robotics, Tianjin University, Tianjin, China
[2]School of Mechanical Engineering, Tianjin Polytechnic University, Tianjin, China
[3]State Key Laboratory of Robotics, Shenyang Institute of Automation, Chinese Academy of Sciences, Shenyang, China
[4]Centre for Robotics Research, School of Physical Sciences and Engineering, King's College, London, UK

Corresponding author:
Rongjie Kang, Key Laboratory of Mechanism Theory and Equipment Design of the Ministry of Education, International Centre for Advanced Mechanisms and Robotics, Tianjin University, Tianjin 300354, China.
Email: rjkang@tju.edu.cn

able to achieve balanced performance for continuum robots in terms of precision, workspace, output forces, etc. SMA is easy to control, but needs time for cooling, which limits its motion frequency. EAP-based actuators have the advantages of light weight but the output displacement and force are relatively small. Hydraulic and pneumatic actuators can generate large displacement and strength with soft structure but lack precision due to the leakage and elasticity of the fluids. Tendon-driven mechanisms are capable of transmitting contracting movement with high resolution, but have low stiffness to take compressive and lateral forces. The use of elastic Ni–Ti rod enhances structural stiffness in the expense of losing compliance.

To improve the capability of continuum robots, hybrid actuation is an effective method. Hošovský et al.[12] proposed a hybrid control scheme for a pair of antagonistically arranged pneumatic muscles. Kang et al.[13] presented a pneumatic muscle-based continuum robot with embedded soft tendons. In such design, the pneumatic muscles provide a majority of the driving force and workspace, and the embedded tendons allow for additional fine adjustment of position. However, the precision of the hybrid actuator is still limited in some directions as the tendons are too soft to withstand compressive and lateral forces. Other hybrid actuators focus on achieving variable stiffness so that the robot maintains compliance to navigate through constrained environments and stiffens itself to resist external disturbances during manipulation. De Falco et al.[14] presented a continuum manipulator for surgery which utilizes granular jamming to realize variable stiffness. Li et al.[15] developed a passive particle jamming principle that needs no vacuum power. However, the use of jamming mechanism will greatly increase the size and weight of the robot body. Shiva et al.[16] proposed a continuum manipulator which utilizes tendons and pneumatic chamber to generate a pair of antagonistic forces to stiffen its body. However, the position and stiffness control of the manipulator are coupled. To solve this problem, Giannaccini et al.[17] proposed a novel design of continuum robot arm which utilizes pneumatic muscles to achieve decoupled variable stiffness and positioning.

The aim of this paper is to find a possible way to blend multiple design requirements for precision, flexibility and workspace in a continuum robot. As mentioned above, pneumatic muscles can achieve large-scale flexible movement, and elastic rods possess higher stiffness to take compressive and lateral forces in comparison with tendons. Thus, they are combined in our design to form a novel hybrid continuum robot in which the pneumatic muscles are used to provide coarse positioning with sufficient flexibility while the elastic rods used for fine positioning with additional structural stiffness. Statics of the continuum robot is then analysed based on an improved Kirchhoff rod model where elastic deformation is calculated by utilizing minimal total potential energy principle in an optimal control framework.

This paper will first introduce the mechanical design and control system of the hybrid continuum robot. Next, static modelling and analysis of the robot will be presented. Then, simulated and experimental validations are carried out, and conclusions are given finally.

Prototype design

In this section, the mechanical design and control system, including a locking mechanism to switch drive modes, of the hybrid continuum robot are presented.

Mechanical design

The continuum robot is composed of two parts, a robotic arm and a driving unit. Figure 1 shows the overview of the robot. The robotic arm consists of three elastic rod embedded pneumatic muscles (eREMs) placed in parallel. The arm will bend if one or two eREMs are pressurized or elongate along its length if all eREMs are pressurized. The connecting plate in the middle of the arm is used to make three eREMs keep parallel when elongating or bending.

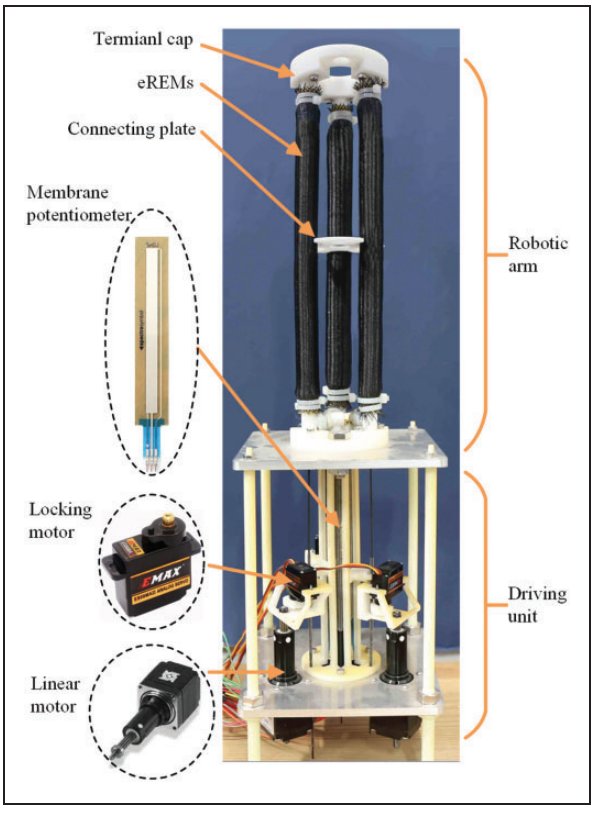

Figure 1. Overview of the robotic prototype. eREM: elastic rod embedded pneumatic muscle.

An eREM is mainly composed of a nylon braided mesh, rubber tube, elastic rod, and pneumatic connector, as shown in Figure 2. The outer nylon braided mesh limits the radial expansion to make the eREM only elongate in the axial direction when inflated.[18] The elastic rod is made of Ni–Ti alloy and fixed to the top of the pneumatic muscle at one end, and passes through the pneumatic connector at the other end (Figure 2). Five blocks are equally spaced on the elastic rod to make it approximately coaxial with the central axis of the pneumatic muscle during bending movement. A rubber seal is placed in the pneumatic connector to prevent air leaking. A membrane potentiometer (Sparkfun, 0.2 mm resolution) is connected to the elastic rod to measure the displacement of the rod, which is equal to the length change of the eREM. The parameters of the eREM are given in Table 1.

There are two drive modes, unlocked mode and locked mode, for such continuum robot. In the unlocked mode, the robotic arm is able to move within a relatively large workspace by purely regulating the air pressure to the eREMs. In the locked mode, accurate positioning with small-scale movement is achieved by retaining the air pressure and using the linear motor (Haydon, 0.003175 mm a step, 4 kg thrust at 300 pulse per second) to push or pull the elastic rod in the longitudinal direction.

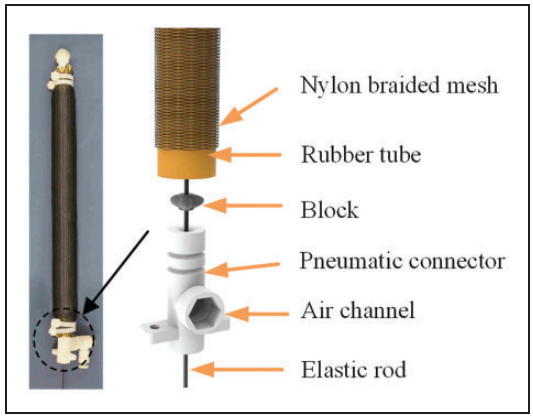

Figure 2. Overview and exploded view of the eREM.

Table 1. Parameters of the eREM.

Parameter	Description	Value	Unit
$\hat{l}$	Initial length of the eREM	200	mm
R	Outer radius of the rubber tube	6.5	mm
r	Radius of the elastic rod	0.5	mm
c	Thickness of the rubber tube	1.5	mm
d	Diameter of the end cap	66	mm
P_{max}	Maximal pressure	0.35	MPa
Δl_{max}	Maximal elongation	48	mm

eREM: elastic rod embedded pneumatic muscle.

There is a mode switching mechanism in the system to enable the elastic rod to work in either active (locked) or passive (unlocked) mode, depending on the task requirement. This mechanism is shown in Figure 3. An oval-shaped cam driven by a locking motor (EMAX ES08MAII) can rotate and push the elastic rod laterally to attach to the 3D-prinnted clamp. Eventually, the rod and clamp will be locked, and the motion of the linear motor is transmitted to the elastic rod via the clamp. This approach requires no additional power once the mechanism is locked. Figure 3(b) and (c) shows the schematic diagram of the unlocked and locked mode, respectively. It is worth mentioning that the rod is coated by a thin layer of silicone in order to increase the friction for reliable locking.

Control system

The topological structure and control architecture of the hybrid actuation are presented in Figures 4 and 5, respectively. It can be seen that each eREM is controlled by a pneumatic regulator or linear motor depending on the selected mode. The host computer sends the desired lengths of the eREMs to the DSP (TMS320F28335) through RS-232 serial link. A DSP reads the data from the potentiometers and generates corresponding control commands to the pneumatic regulators (SMC ITV1051), linear motors, and locking motors. A proportional–integral–derivative (PID) algorithm is used to control the length of the eREMs.

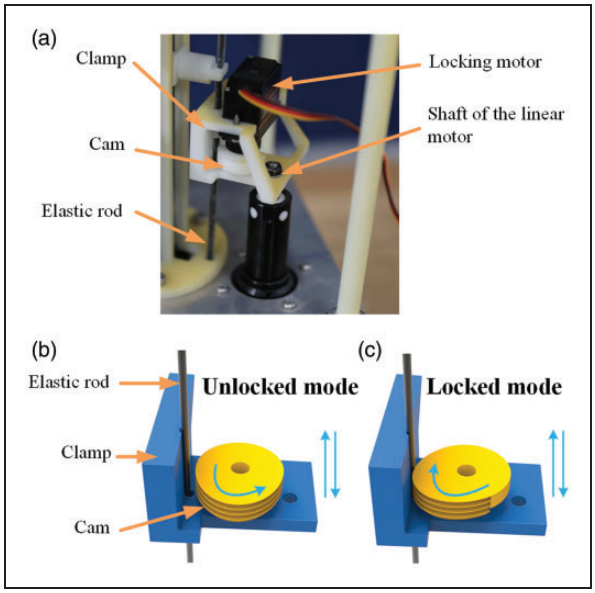

Figure 3. Mode switching mechanism: (a) the prototype; (b) the unlocked mode: the cam does not attach to the elastic rod, so the linear motion of the clamp cannot be transmitted to the elastic rod; and (c) the locked mode: the cam locks the elastic rod to the clamp so they will move together.

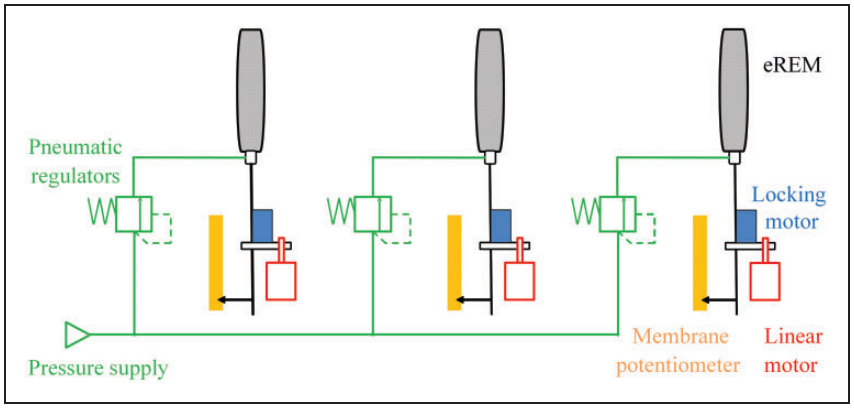

Figure 4. Topological structure of the hybrid actuation.
eREM: elastic rod embedded pneumatic muscle.

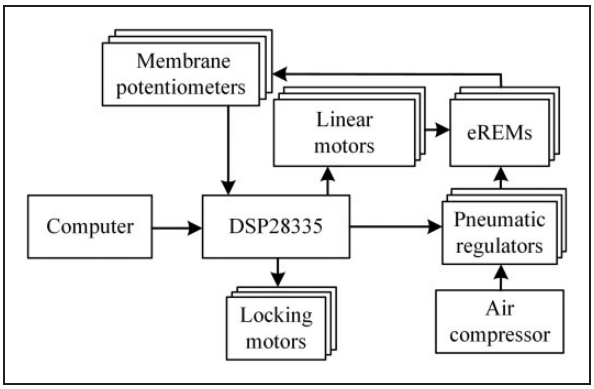

Figure 5. The control architecture.
eREM: elastic rod embedded pneumatic muscle.

The control logic for a single eREM is presented in Figure 6. The desired length of the eREM will be compared with the actual length. If the error is greater than a preset threshold, the eREM will be inflated or deflated to coarsely tune its length. When the length error is equal to or smaller than the threshold, the locking motor will be activated to lock the elastic rod to the linear motor for fine tuning of the length. A large threshold will lead to premature use of the rod actuation, and therefore reduces the response speed and increases the internal force. However, a small threshold may lose efficacy because the pneumatic muscle actuation has relatively large positioning error and may never reach the threshold. In our prototype, the positioning error of the pneumatic muscle is about 3 mm, thus, the threshold is set to 5 mm.

Modelling and analysis

In this section, the statics of the continuum robot is presented based on an improved Kirchhoff rod model and solved with an optimal control method using the minimal total potential energy principle.

Improved Kirchhoff rod model

In this paper, we focus on investigating the linear and bending deformation of the robot resulting from the actuating and external forces. Twist and shear deformation are not considered as they are relatively small in comparison with the linear and bending deformation.[19] Also, due to the presence of the connecting plate, three eREMs are assumed parallel to a virtual backbone along the central axis of the robot as shown in Figure 7(a). The deformation of the robot can be represented by the deformation of the virtual backbone.[20]

A general Kirchhoff rod model considers a rod has a constant length, and it uses the curvature at each point on the rod to characterize its deformation.[21] Note that, the backbone of the presented robot can elongate or contract, thus, an improved Kirchhoff rod model with both axial strain and curvature is developed here.

An arc coordinate system O–t and a Cartesian coordinate system O–xyz are established on the virtual backbone, as shown in Figure 7(b). The solid blue curve is the backbone, and the dotted ones are the projections of the backbone on the x–O–y, x–O–z, and y–O–z planes, respectively. The arc length is represented by $t \in [0, t_f]$ where $t = t_f$ refers to the top end of the backbone. As the backbone and eREMs are parallel, such backbone curve can also represent the shape of the eREMs. A state vector of the backbone and eREMs is then defined as

$$\boldsymbol{V}_i(t) = \begin{bmatrix} x_i(t) & y_i(t) & z_i(t) & \tau_i(t) & \xi_i & \theta_i(t) \end{bmatrix}^T \quad (1)$$

where $i = 0, 1, 2, 3$ is the index number of the backbone and eREMs, Figure 7(a). $x_0(t)$, $y_0(t)$, and $z_0(t)$ are coordinates of a point A with arc length t on the backbone. $\tau_0(t)$, ξ_0, and $\theta_0(t)$ are the angles of the tangent projections at point A about the coordinate axes (Figure 7(b)). These parameters have the same meaning for eREMs ($i = 1,2,3$). The axial deformation of the backbone and eREMs are described by the

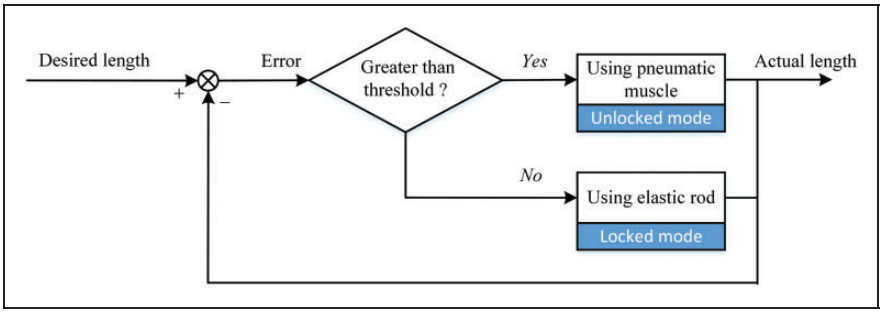

Figure 6. The control logic for a single eREM.

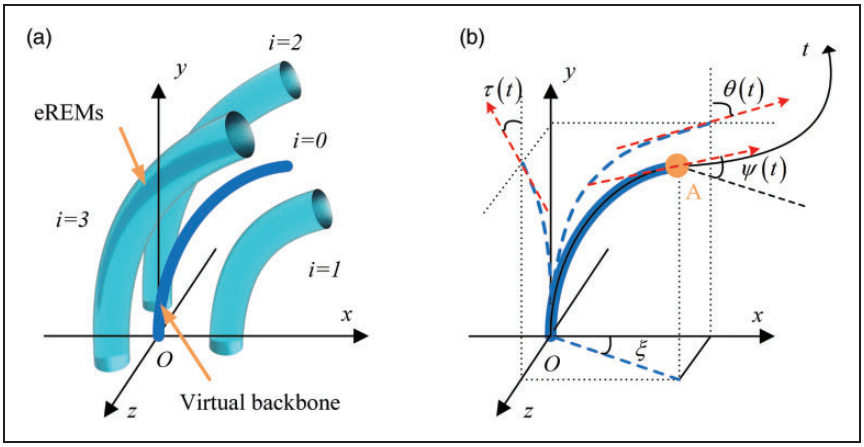

Figure 7. Establishment of the coordinate systems: (a) virtual backbone and (b) arc coordinate system and the state angles. eREM: elastic rod embedded pneumatic muscle.

axial elongation rate $\eta_i(t) = \left(l_i - \hat{l}\right)/\hat{l}$, where l_i is the actual length of eREMs and $\hat{l}$ is the initial length. $\eta_i(t) > 0$ means elongation and $\eta_i(t) < 0$ means contraction.

Optimal control method

The posture of the presented robot is related to the length of the eREMs and the external load applied to the robot. In this paper, the length of an eREM can be described by the aforementioned axial elongation rate $\eta_i(t)$ which is determined by the air pressure or linear motor depending on the drive mode. Also, we only consider the external load is applied to the terminal of the robot. From a control point of view, the length of an eREM is an active control input to the robot while the terminal load is an external disturbance. According to the principle of minimal total potential energy, when the lengths of the eREMs and the terminal load are given, the final deformation of the eREMs will ensure the overall potential energy of the system minimum, including the strain energy, the potential of air pressure, and the potential of external loads.[22] Therefore, the problem of finding the deformation of eREMs and virtual backbone can be regarded as an optimal control problem to minimize the energy of the system.[21] This method is mathematically concise and minimally affected by discretization issues compared with the lumped-parameter and finite element approaches.[23] In this paper, an optimal control method based on the principle of minimal total potential energy is utilized to solve the improved Kirchhoff rod model.

In Figure 7(b), the derivative of the state vector at point A with respect to the arc length, t, is

$$\dot{\boldsymbol{V}}_i(t) = f_i(\boldsymbol{V}, \boldsymbol{U}, t) = \begin{bmatrix} [1+\eta_i(t)]\cos\psi_i(t)\cos\xi_i \\ [1+\eta_i(t)]\sin\psi_i(t) \\ [1+\eta_i(t)]\cos\psi_i(t)\sin\xi_i \\ \chi_i(t) \\ 0 \\ \omega_i(t) \end{bmatrix} \tag{2}$$

where $\psi_i(t)$ is the pitch angle between tangent direction and the x–O–z plane. $\boldsymbol{U}$ is defined as a deformation vector including elongation rate $\eta_i(t)$ and curvatures $\chi_i(t)$, $\omega_i(t)$ about the x and z axes, respectively

$$\boldsymbol{U}_i(t) = \begin{bmatrix} \eta_i(t) & 0 & 0 & \chi_i(t) & 0 & \omega_i(t) \end{bmatrix}^T \tag{3}$$

where the second and third items are zero meaning that the shear deformation is not considered in the model. Similarly, the fifth item means the twists are neglected as assumed previously. The terminal load is assumed to be applied to the top end of the backbone and written in the form of a vector as

$$\boldsymbol{W} = \begin{bmatrix} F_x & F_y & F_z & M_x & M_y & M_z \end{bmatrix}^T \tag{4}$$

where F_x, F_y, F_z are the components of the load force along the x, y, and z axes, and M_x, M_y, M_z are the components of the load torque about the x, y, and z axes.

According to the deformation vector $\boldsymbol{U}$, the eREM's stiffness vector is

$$\boldsymbol{K} = \begin{bmatrix} K_1 & 0 & 0 & K_2 & 0 & K_2 \end{bmatrix}^T \tag{5}$$

where K_1 is the axial stiffness per unit length of the eREM and K_2 is the bending stiffness per unit length of the eREM. The values of these two parameters will be calculated in the following section. The strain energy density of the eREMs can be written as

$$\sum_{i=1}^{3} L_i(\boldsymbol{V}, \boldsymbol{U}, t) = \sum_{i=1}^{3} \frac{1}{2} \boldsymbol{U}_i^T(t) \boldsymbol{K} \boldsymbol{U}_i(t) \tag{6}$$

The potential energy density of air pressure in the eREMs is written as

$$G_i(\eta_i) = -P_i S \eta_i \tag{7}$$

where P_i is the air pressure in the eREM and $S = \pi(R-c)^2$ is the cross-sectional area of the air chamber in the eREMs. So the total energy of the system is

$$J = \phi(\boldsymbol{V}_{0f}) + \int_0^{t_f} \sum_{i=1}^{3} [L_i(\boldsymbol{V}, \boldsymbol{U}, t) + G_i(\eta_i)] \, \mathrm{d}t \tag{8}$$

The first item $\phi(\boldsymbol{V}_{0f}) = -\boldsymbol{W}^T \boldsymbol{V}_0(t_f)$ is the potential of the terminal loads and the second item $\int_0^{t_f} \sum_{i=1}^{3} [L_i(\boldsymbol{V}, \boldsymbol{U}, t) + G_i(\eta_i)] \, \mathrm{d}t$ is the sum of the elastic potential energy and the potential of air pressure in the three eREMs. From an optimal control point of view, to find the deformation of the eREMs is equivalent to find a deformation vector $\boldsymbol{U}$ to minimize the energy of the system, so the statement of the problem is

$$\begin{aligned} &\underset{\mathbf{U}(t)}{\text{minimize}} \; J = \phi(\boldsymbol{V}_{0f}) + \int_0^{t_f} \sum_{i=1}^{3} [L_i(\boldsymbol{V}, \boldsymbol{U}, t) + G_i(\eta_i)] \, \mathrm{d}t \\ &\text{subject to } \dot{\boldsymbol{V}}_i = f_i(\boldsymbol{V}, \boldsymbol{U}, t) \\ &\qquad \boldsymbol{V}_i(0) = \boldsymbol{V}_{i0} \end{aligned} \tag{9}$$

The Hamiltonian H and the Lagrange multiplier λ are introduced as

$$H_i(\boldsymbol{V}, \boldsymbol{U}, \boldsymbol{\lambda}, t) = L_i(\boldsymbol{V}, \boldsymbol{U}, t) + G_i(\eta_i) + \boldsymbol{\lambda}_i^T(t) f_i(\boldsymbol{V}, \boldsymbol{U}, t) \tag{10}$$

where $\boldsymbol{\lambda}_i$ is a 6×1 vector with physical meaning. $\boldsymbol{\lambda}_{i,1}(t)$, $\boldsymbol{\lambda}_{i,2}(t)$, $\boldsymbol{\lambda}_{i,3}(t)$ are the internal force vectors along the x, y, and z axes and $\boldsymbol{\lambda}_{i,4}(t)$, $\boldsymbol{\lambda}_{i,5}(t)$, $\boldsymbol{\lambda}_{i,6}(t)$ are the internal torque vectors.[24] So equation (8) can be rewritten as

$$\begin{aligned} \hat{J} = \phi(\boldsymbol{V}_{0f}) + \int_0^{t_f} \sum_{i=1}^{3} & H_i[\boldsymbol{V}(t), \boldsymbol{U}, \boldsymbol{\lambda}, t] \\ & - \boldsymbol{\lambda}_i^T(t) f_i[\boldsymbol{V}(t), \boldsymbol{U}, t] \, \mathrm{d}t \end{aligned} \tag{11}$$

Discrete model

In order to solve the above model numerically, a discrete model is necessary. The virtual backbone is equally divided into N segments. Figure 8 shows an enlarged view of adjacent three segments. As long as the segment is short, it can be approximately considered that the curvature of each segment remains constant in one segment. For the convenience of calculation, it is assumed that the elastic potential energy of the kth segment is stored in the kth node. The state vectors of the nodes on the backbone and eREMs are represented by using $\boldsymbol{V}_i(k)$, thus, equation (11) can be rewritten as

$$\begin{aligned} \hat{J} = \phi[\boldsymbol{V}_0(N+1)] + \sum_{k=1}^{N} \sum_{i=1}^{3} \big\{ & H_i[\boldsymbol{V}(k), \boldsymbol{U}(k), \boldsymbol{\lambda}, k] \\ & - \lambda_i^T(k) f_i[\boldsymbol{V}(k), \boldsymbol{U}, k] \big\} \end{aligned} \tag{12}$$

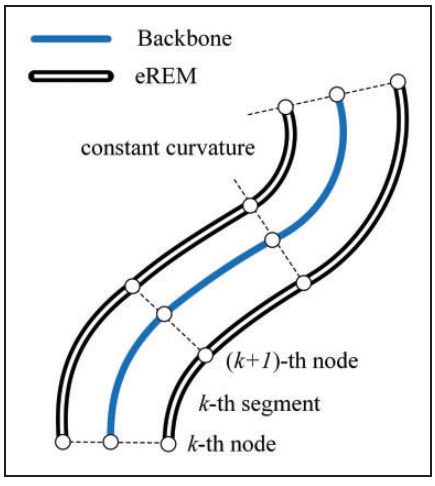

Figure 8. The discretization of virtual backbone and eREMs. eREM: elastic rod embedded pneumatic muscle.

Define the Hamiltonian of robot as

$$H_0[\boldsymbol{V}(k), \boldsymbol{U}, \boldsymbol{\lambda}, k] = \sum_{i=1}^{3} \{L_i[\boldsymbol{V}(k), \boldsymbol{U}, k] + G_i(\eta_i)\} + \boldsymbol{\lambda}_0^T(k) f_0[\boldsymbol{V}(k), \boldsymbol{U}, k] \quad (13)$$

where $\boldsymbol{\lambda}_0(k)$ is the resultant internal forces (torques) of the three eREMs on the cross-section of the kth node.

In accordance with the optimal control principle,[25] when the total energy is minimum, the following conditions are satisfied

$$\begin{aligned} \dot{\boldsymbol{V}}_0(k) &= \frac{\partial H_0[\boldsymbol{V}(k), \boldsymbol{U}, \boldsymbol{\lambda}, k]}{\partial \boldsymbol{\lambda}_0(t)} = f_0[\boldsymbol{V}(k), \boldsymbol{U}, k] \\ \dot{\boldsymbol{\lambda}}_0(k) &= -\frac{\partial H_0[\boldsymbol{V}(k), \boldsymbol{U}, \boldsymbol{\lambda}, k]}{\partial \boldsymbol{V}_0(k)} \\ \boldsymbol{\lambda}_0(N+1) &= \frac{\partial \phi(N+1)}{\partial \boldsymbol{V}_0(N+1)} \\ & \frac{\partial H_0[\boldsymbol{V}(k), \boldsymbol{U}, \boldsymbol{\lambda}, k]}{\partial \boldsymbol{U}_0(k)} = 0 \end{aligned} \quad (14)$$

Solving equation (14) can obtain the deformation vector $\boldsymbol{U}_0(k)$ including elongation rate $\eta_0(k)$, curvature vectors $\chi_0(k)$, $\omega_0(k)$. By integrating them, the state vector of the backbone nodes $\boldsymbol{V}_0(k)$ can be calculated, and the robot's entire deformation is obtained.

eREM stiffness

In this section, the parameters of the stiffness vector $\boldsymbol{K}$ in equation (5) are calculated. There are two kinds of stiffness in the vector, i.e. the axial and bending stiffness per unit length of the eREM.

An eREM is composed of a braided mesh, a rubber tube, and an elastic rod in parallel. Therefore, its axial stiffness is the sum of all elements. Note that, the elastic rod will move passively with the pneumatic muscle in the unlocked mode, which means it does not contribute axial stiffness to the system in this mode. Thus, according to the theory of material mechanics,[26] the axial stiffness per unit length of the eREM is

$$\begin{cases} K_1 = lk_{\text{mesh}} + E_{\text{rubber}} A_{\text{rubber}} + E_{\text{rod}} A_{\text{rod}} & \text{(locked mode)} \\ K_1 = lk_{\text{mesh}} + E_{\text{rubber}} A_{\text{rubber}} & \text{(unlocked mode)} \end{cases} \quad (15)$$

where E is the Young's modulus and A is the cross-sectional area. k_{mesh} is the stiffness of the braided mesh. Leclair et al.[27] and Doumit et al.[28] proposed the expression of k_{mesh} as

$$k_{\text{mesh}} = \frac{\mathrm{d}F_{\text{mesh}}}{\mathrm{d}l} = -\frac{\mathrm{d}P}{\mathrm{d}l}\left[\frac{l_y^2 - 3l^2}{4\pi n^2}\right] + \frac{3Pl}{2\pi n^2} \quad (16)$$

where F_{mesh} is the axial force of the braided mesh in the condition that the pneumatic muscle is inflated, l_y is the length of the uncoiled nylon fibre composing the braided mesh, and n is the number of revolutions of the nylon fibre around the pneumatic muscle.

The bending stiffness of the eREM is also a sum of all elements. Bending stiffness per unit length of the eREM can be written as

$$K_2 = \frac{lk_{\text{mesh}}}{A_{\text{mesh}}} I_{\text{mesh}} + E_{\text{rubber}} I_{\text{rubber}} + E_{\text{rod}} I_{\text{rod}} \quad (17)$$

where I is the moment of inertia and A is the cross-sectional area. Equation (17) is valid for both locked and unlocked modes.

Experimental validation

Model validation

The interpolation method[11] is used here to estimate the deformation of the robotic arm which is characterized by three reference points along the length of one eREM, as shown in Figure 9(a). The positions of the reference points are measured by a 3D tracking system (3D Guidance trakSTAR, NDI). The measurement error of the tracking system is below 1.0 mm. In order to reduce the influence of measurement error, each reference point is measured for

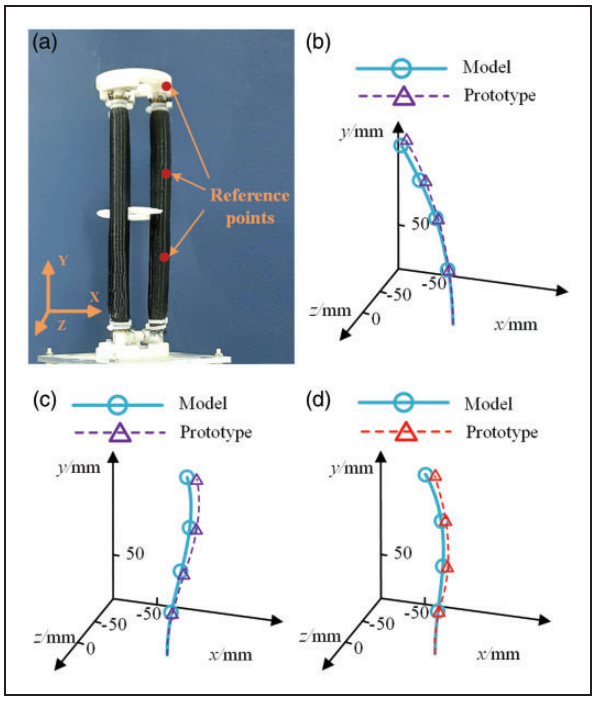

Figure 9. Comparison of the model and robotic prototype: (a) Placement of the sensors on the prototype, (b) experiment in the unlocked mode without a terminal load, (c) experiment in the unlocked mode with a terminal load, and (d) experiment in the locked mode with a terminal load.

5 times, and their average is used as the actual position of the reference point. In this paper, a root-mean-square error (RMSE) is adopted to describe the gap between the presented model and robotic prototype as

$$RMSE = \sqrt{\frac{\sum_{m=1}^{3}\left[\left(x_m - x'_m\right)^2 + \left(y_m - y'_m\right)^2 + \left(z_m - z'_m\right)^2\right]}{3}} = \sqrt{\frac{\sum_{m=1}^{4}\varepsilon_m^2}{3}} \quad (18)$$

where $\begin{bmatrix} x'_m & y'_m & z'_m \end{bmatrix}^T$ is the position of the reference point obtained by the model and $\begin{bmatrix} x_m & y_m & z_m \end{bmatrix}^T$ is the position of the reference point measured from the prototype.

The presented model will be validated in three cases: (a) bending motion actuated by air pressure without terminal load in the unlocked mode, (b) bending motion actuated by air pressure with terminal load in the unlocked mode, and (c) bending motion actuated by air pressure with terminal load in the locked mode.

In case a, the eREMs are inflated with air pressure of 200 kPa ($i = 1$) and 50 kPa ($i = 2,3$), respectively. Other parameters of the prototype for simulation are listed in Table 2 where the superelastic material Ni–Ti is assumed to have an isotropic and constant Young's modulus.[29] After comprehensively considering the computational time and the precision, the number of segments $N = 10$ is selected. Substituting above parameters into equation (14), it can be solved that $\eta_1 = 0.202$, $\eta_2 = \eta_3 = 0.069$, $\chi_0 = 0$, $\omega_0 = 3.477$ rad/m. The deformation vector $\mathbf{U}_0(k)$ at each node on the eREMs is the same. The comparison between the model and prototype is shown in Figure 9(b). It can be seen that the position errors at the reference points increase from 1.4 to 7.6 mm along the robotic arm from the base to tip. The RMSE is 4.23 mm (2.1% of the initial length of the robotic arm).

In case b, the input pressures for the eREMs are the same as that in case a. A 1 N horizontal force along the x axis is then applied to the terminal of the robotic prototype. Simulation and experimental results are shown in Figure 9(c). It was found that the position error increases from 2.4 to 13.7 mm. The RMSE at these points is 9.38 mm (4.7% of the initial length of the robotic arm).

In case c, we first inflated the eREMs with the same pressure, then switched the system to the locked mode and applied a horizontal force of 1 N again. The experimental result and simulation are shown in Figure 9(d) and the RMSE is 6.35 mm (3.2% of the initial length of the robotic arm).

It can be concluded that either in the unlocked or locked mode, the simulated results almost agree with the experimental results. Therefore, the model established in this paper is effective. The errors are mainly due to the uncertainties in the simulated parameters and the frictions that are not accounted for in the model.

Variable stiffness of the robot

In this paper, the stiffness of the robotic arm is defined as

$$K_{\text{robot}} = \frac{F_e}{\Delta s} \quad (19)$$

where Δs is the displacement of the terminal of the robotic arm due to the applied force F_e in the x direction. This parameter reflects the resistance of the robotic arm to the deformation caused by external force. In our experiment, three cases with different eREM inputs were used to verify the variable stiffness of the robotic arm. The input air pressure for the eREMs is listed in Table 3. For each case, external force $F_e = 2.5$ N was applied to the terminal of the

Table 3. Inputs to the eREMs.

Case	P_1 (kPa)	P_2 (kPa)	P_3 (kPa)
1	150	50	50
2	50	50	50
3	50	150	150

eREM: elastic rod embedded pneumatic muscle.

Table 2. Parameters used in simulation.

Parameter	Description	Value	Unit
n	The number of fibre revolutions in the eREM	9	–
E_{rubber}	Young's modulus of the rubber tube	1.45	MPa
E_{rod}	Young's modulus of the elastic rods (martensite)	28	GPa
I_{mesh}	The area moment of inertia of the mesh	483.5×10^{-12}	m^4
I_{rubber}	The area moment of inertia of the rubber tube	1079.375×10^{-12}	m^4
I_{rod}	The area moment of inertia of the elastic rod	0.049×10^{-12}	m^4

eREM: elastic rod embedded pneumatic muscle.

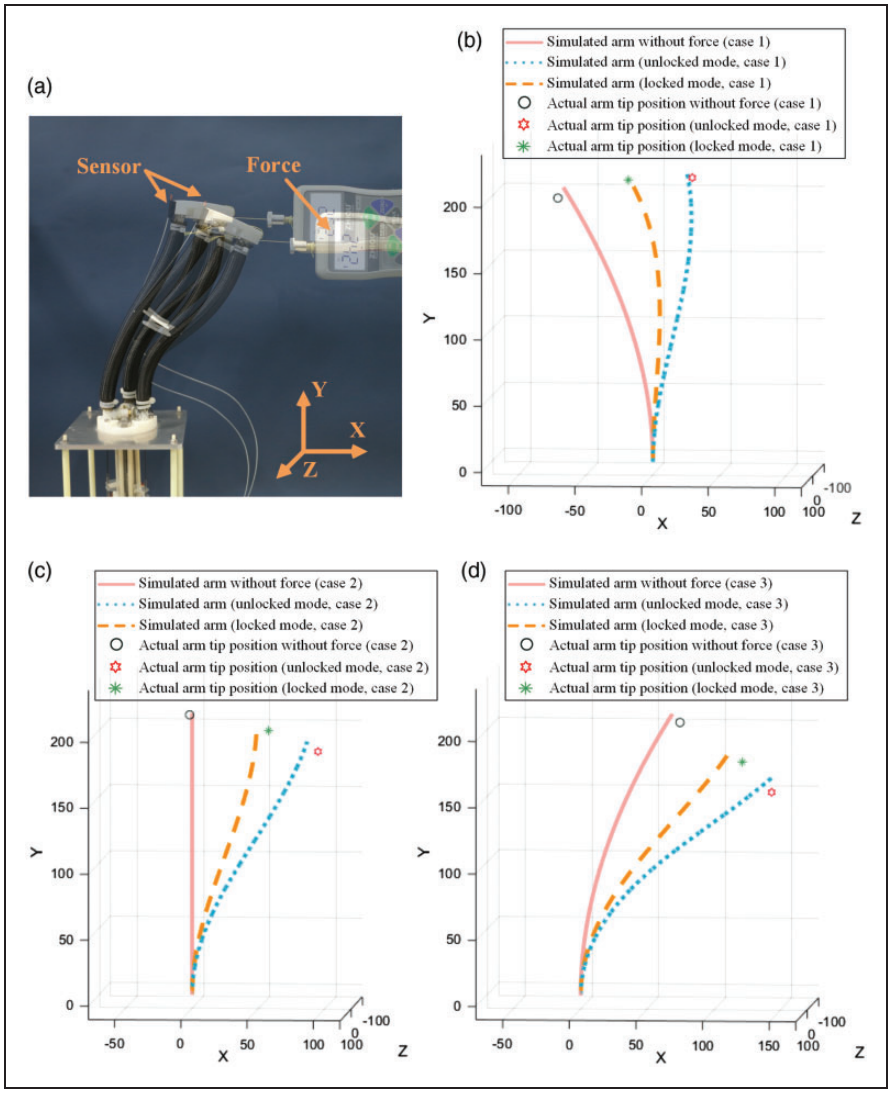

Figure 10. Variable stiffness: (a) experimental setup, (b) comparison of the simulated and experimental results in case 1, (c) comparison of the simulated and experimental results in case 2, and (d) comparison of the simulated and experimental results in case 3.

robotic arm in the unlocked and locked mode, respectively.

Setup of the experimental platform is shown in Figure 10(a). Simulated and experimental results are compared in Figure 10(b) to (d) and listed in Table 4. It can be seen that in all cases the stiffness obtained from experiments was significantly increased in the locked mode by around 65.1% averagely compared to those in the unlocked mode. The stiffness in case 2 was smaller than that in cases 1 and 3. This is because the initial state of the robotic arm in case 2 was vertical and the horizontal external force was completely transformed into the bending moment resulting in larger lateral displacement Δs. If the Young's modulus of the elastic rod increases, the lateral displacement Δs under external force F_e will decrease, and therefore the system will behave more like a rigid one. We also noticed that the actual stiffness measured from the experiment is generally less than the theoretical stiffness obtained from the model. There are probably two reasons for this. One reason is the eREMs have air leakage in the pneumatic connector, which may reduce its axial and bending stiffness. The other reason is the gravity of the robotic arm which is neglected in the model. Therefore, the actual displacement of the robotic arm terminal in the experiment is greater than that in the simulation.

Repeatability of the robot

To observe the repetitive positioning error of the robot in two drive modes, a tracking sensor is mounted at the terminal of the robotic arm. The tests were conducted under two conditions. In case A, the desired lengths of the eREMs are set to 230 mm ($i=1$) and 210 mm ($i=2,3$) while in case B the desired lengths of the eREMs are set to 210 mm ($i=1$) and 230 mm ($i=2,3$). For each case, the tests were repeated by 10 times in the unlocked and locked mode, respectively. In this experiment, there is no

Table 4. Experimental results of arm deformation.

Case	Drive mode	Simulation			Experiment		
		Δs (mm)	K_{robot} (N/m)	Stiffness change (%)	Δs (mm)	K_{robot} (N/m)	Stiffness change (%)
1	Unlocked	88.08	28.38	–	97.01	25.77	–
	Locked	49.94	50.06	76.40	52.77	47.38	83.86
2	Unlocked	91.90	27.20	–	98.93	25.27	–
	Locked	50.68	49.33	81.36	59.79	41.81	65.45
3	Unlocked	73.62	33.96	–	68.91	36.27	–
	Locked	46.60	53.65	57.98	47.14	53.03	46.21

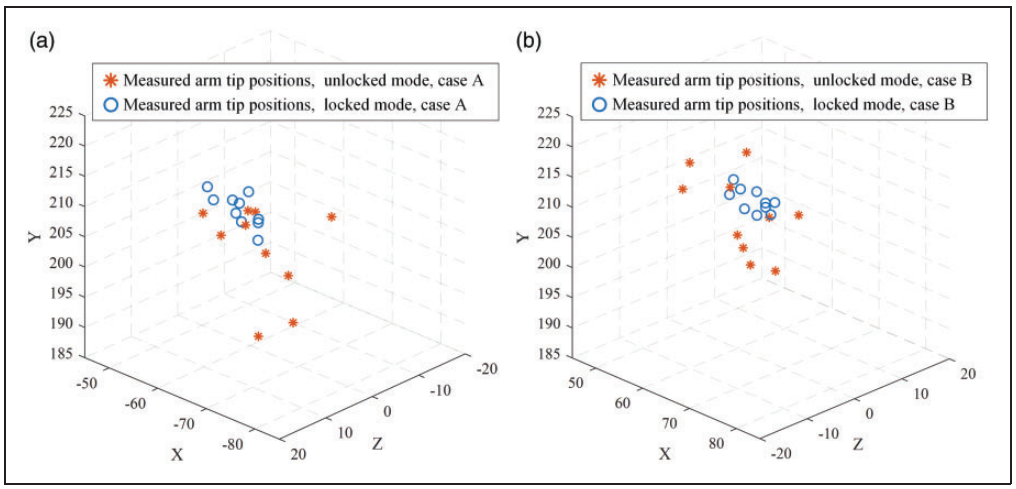

Figure 11. The distribution of the arm tip positions measured from the repetitive tests: (a) case A and (b) case B.

Table 5. Standard deviation of the arm tip position along each axis.

Case	Drive mode	x (mm)	y (mm)	z (mm)	Average reduction (%)
A	Unlocked	6.63	5.78	6.36	–
	Locked	3.26	1.96	1.77	63.03
B	Unlocked	5.71	5.24	5.32	–
	Locked	2.80	1.80	1.53	62.62

terminal load applied to the robot tip. The robot adopts PID-based closed-loop controller to tune the lengths of the individual eREMs with the help of the membrane potentiometers. The results are plotted in Figure 11. In all cases, dispersion of the robot terminal was observed. This is because of some uncertainties in the robot such as air leakage, friction, hysteresis, and measurement errors.

Whether in case A or case B, a qualitative conclusion can be made that in the unlocked mode, the positions of the robotic arm tip are more scattered, and in the locked mode, the positions are more concentrated. The standard deviation of these points is listed in Table 5. It can be seen that the standard deviation has an average reduction around 62.8% in the locked mode, which means the hybrid actuation is beneficial to the repeatability of the robot. This is because the structure stiffness of the robot improves in the locked mode.

Conclusions

In this paper, we put forward a novel hybrid continuum robot that can switch drive mode between pneumatic muscles and elastic rods to change its structural stiffness and achieve balanced performance in flexibility and precision. An improved Kirchhoff rod model is formulated to describe the statics of the robot and solved in an optimal control framework by using the minimal total potential energy principle. Finally, simulated and experimental results show that the presented static model has good consistency with the prototype and the hybrid robot can increase its structural stiffness by 65.1% when performing fine positioning in the locked mode and reduce the repetitive positioning error by 62.8%. Future work will investigate the Jacobian of the robot to reveal the kinematic relationship between individual eREMs

and the end point of the robot. Also, the robotic prototype will be extended to a multi-segmented case that allows for greater workspace and flexibility.

Declaration of Conflicting Interests

The author(s) declared no potential conflicts of interest with respect to the research, authorship, and/or publication of this article.

Funding

The author(s) disclosed receipt of the following financial support for the research, authorship, and/or publication of this article: The authors are grateful for the financial support from the Natural Science Foundation of China (Grant No. 51875393, 51605329, 51535008, and 51721003), International Collaboration Programme No. B16034, and the Tianjin Municipal Science and Technology Department Programme (Grant No. 17JCQNJC03600).

References

1. Guglielmino E, Tsagarakis N and Caldwell D. An octopus anatomy-inspired robotic arm. In: *IEEE/RSJ international conference on intelligent robots and systems (IROS)*, Taipei, Taiwan, 2010, pp.3091–3096.
2. Jones B and Walker I. Practical kinematics for real-time implementation of continuum robots. *IEEE Trans Robot* 2006; 22: 1087–1099.
3. Menciassi A, Gorini S, Pernorio G, et al. A SMA actuated artificial earthworm. In: *IEEE international conference on robotics and automation (ICRA)*, New Orleans, LA, USA, 2004, pp.3282–3287.
4. Shintake J, Rosset S, Schubert B, et al. Polymer actuators: versatile soft grippers with intrinsic electroadhesion based on multifunctional polymer actuators. *Adv Mater* 2016; 28: 231.
5. Yuk H, Lin S, Ma C, et al. Hydraulic hydrogel actuators and robots optically and sonically camouflaged in water. *Nat Commun* 2017; 8: 14230.
6. Walker I, Dawson D, Flash T, et al. Continuum robot arms inspired by cephalopods. In: *The proceedings of the 2005 SPIE conference on unmanned ground vehicle technology IV*, Bellingham, WA, USA, 2005, pp.303–314.
7. Kang R, Branson D, Zheng T, et al. Design, modeling and control of a pneumatically actuated manipulator inspired by biological continuum structures. *Bioinsp Biomim* 2013; 8: 036008.
8. Robertson M and Paik J. New soft robots really suck: vacuum-powered systems empower diverse capabilities. *Sci Robot* 2017; 2: eaan6357.
9. Calisti M, Giorelli M, Levy G, et al. An octopus-bioinspired solution to movement and manipulation for soft robots. *Bioinsp Biomim* 2011; 6: 036002.
10. Cao K, Kang R, Branson D, et al. Workspace analysis of tendon-driven continuum robots based on mechanical interference identification. *J Mech Des* 2017; 139: 062303.
11. Xu K and Simaan N. Actuation compensation for flexible surgical snake-like robots with redundant remote actuation. In: *IEEE international conference on robotics and automation (ICRA)*, Orlando, Florida, USA, 2006, pp.4148–4154.
12. Hošovský A, Marcinčin J, Piteľ J, et al. Model-based evolution of a fast hybrid fuzzy adaptive controller for a pneumatic muscle actuator. *Int J Adv Robot Syst* 2012; 9: 1.
13. Kang R, Guo Y, Chen L, et al. Design of a pneumatic muscle based continuum robot with embedded tendons. *IEEE/ASME Trans Mechatron* 2017; 22: 751–761.
14. De Falco I, Cianchetti M and Menciassi A. A soft multi-module manipulator with variable stiffness for minimally invasive surgery. *Bioinsp Biomim* 2017; 12(5): 056008.
15. Li Y, Chen Y, Yang Y, et al. Passive particle jamming and its stiffening of soft robotic grippers. *IEEE Trans Robot* 2017; 33: 446–455.
16. Shiva A, Stilli A, Noh Y, et al. Tendon-based stiffening for a pneumatically actuated soft manipulator. *IEEE Robot Autom Lett* 2016; 1: 632–637.
17. Giannaccini M, Xiang C, Atyabi A, et al. Novel design of a soft lightweight pneumatic continuum robot arm with decoupled variable stiffness and positioning. *Soft Robot* 2018; 5: 54–70.
18. Pritts M and Rahn C. Design of an artificial muscle continuum robot. In: *IEEE international conference on robotics and automation (ICRA)*, New Orleans, LA, USA, 2004, pp.4742–4746.
19. Rone W and Ben-Tzvi P. Continuum robot dynamics utilizing the principle of virtual power. *IEEE Trans Robot* 2014; 30: 275–287.
20. Rone W and Ben-Tzvi P. Mechanics modeling of multisegment rod-driven continuum robots. *J Mech Robot* 2014; 6: 041006.
21. Bretl T and Mccarthy Z. Quasi-static manipulation of a Kirchhoff elastic rod based on a geometric analysis of equilibrium configurations. *Int J Robot Res* 2013; 33: 48–68.
22. Reddy J. *Energy principles and variational methods in applied mechanics*. 2nd ed. Hoboken, New Jersey, USA: John Wiley & Sons, 2002.
23. Till J and Rucker D. Elastic stability of cosserat rods and parallel continuum robots. *IEEE Trans Robot* 2017; 33: 718–733.
24. Antman S, Marsden J and Sirovich L. *Nonlinear problems of elasticity*. 2nd ed. Berlin/Heidelberg, Germany: Springer Science, 2005.
25. Berkovitz LD. *Optimal control theory*. Berlin/Heidelberg, Germany: Springer Science & Business Media, 2013.
26. Liu H. *Material mechanics*. Beijing, China: China Higher Education Press, 2004.
27. Leclair J, Doumit M and McAllister G. Analytical stiffness modeling and experimental validation for a pneumatic artificial muscle. In: *ASME international mechanical engineering congress and exposition*, Montreal, Quebec, Canada, 2014, p.V009T12A089.
28. Doumit M, Fahim A and Munro M. Analytical modeling and experimental validation of the braided pneumatic muscle. *IEEE Trans Robot* 2009; 25: 1282–1291.
29. Xu K and Simaan N. Analytic formulation for kinematics, statics, and shape restoration of multibackbone continuum robots via elliptic integrals. *J Mech Robot* 2010; 2: 011006.